**Biogeosciences
Discussions**

A two-dimensional model of the methane cycle in a sedimentary accretionary wedge

D. E. Archer[1] and B. A. Buffett[2]

[1]Department of Geophysics, University of Chicago, Chicago, IL, USA
[2]Department of Earth and Planetary Sciences, University of California, Berkeley, CA, USA

Correspondence to: D. Archer (d-archer@uchicago.edu)

Abstract

A two-dimensional model of sediment column geophysics and geochemistry has been adapted to the problem of an accretionary wedge formation, patterned after the margin of the Juan de Fuca plate as it subducts under the North American plate. Much of the model description was given in a companion paper about application of the model to a passive margin setting; here we build on that formulation to simulate the deformation of the sediment wedge as it approaches the subduction zone. The active margin configuration of the model shares sensitivities with the passive margin configuration, in that sensitivities to organic carbon deposition and respiration kinetics, and to vertical bubble transport and redissolution in the sediment, are stronger than the sensitivity to ocean temperature. The active margin simulation also shows a sensitivity to plate subduction velocity, with higher plate velocities producing less hydrate per meter of coastline than slower velocities or the passive margin configuration. However, the local hydrate concentrations, as pore volume saturation, are higher in the active setting than the passive, as generally observed in the field.

1 Introduction

Most models of methane hydrate cycling in the sediment column of the ocean are formulated to mimic the "stratographic" hydrate deposits (Milkov, 2004), which comprise most of the hydrate reservoir. There have been fewer models of the methane cycle in accretionary wedge sediment complexes, because of the greater complexity of the underlying physics (Carson et al., 1990): instead of ongoing sediment accumulation onto a collapsing but essentially one-dimensional sediment column, in an accretionary wedge complex the sediment is actively deformed by compression associated with the scrape-off of the sediment complex from the underlying subducting oceanic crust. An accretionary wedge sediment complex is an example of a "structural" hydrate deposit, which comprise a smaller fraction of the hydrate inventory globally but which form hy-

drate in higher concentrations, even forming massive hydrate blocks, and forming them closer to the sediment surface than the stratigraphic deposits, which tend to concentrate hydrate at the base of the stability zone, often hundreds of meters below the sea floor. In particular, the model is applied to the case of the Cascadia margin (Spence et al., 2000).

2 Overview of the passive margin configuration

Called SpongeBOB, the numerical model is described in a companion paper (Archer et al., 2012) as it was formulated for a passive continental margin setting. The model formulation as described in that paper will be summarized here before we show details of the additional model formulation required for the accretionary wedge setting. The model is formulated on a two-dimensional grid, onshore/offshore in the lateral dimension and with a stretching "sigma" grid in the vertical. The model is intended to span the continental margin from the continent to the abyss, over geologic time scales of 10^7–10^8 years.

2.1 Sediment transport

A sediment transport scheme distributes material to the sea floor. Continental material originates at the left-hand (continental) side of the domain, and is transported and sedimented according to the sinking velocities of the various grain sizes, and the water depth (which prevents sedimentation if it is too shallow). Another fraction of the sedimenting material is called "pelagic", and it deposits uniformly throughout the domain, if the water is deep enough. When the slope of the sea floor exceeds a critical value set at 4–6 % grade, sediment resuspends and is distributed downslope. This material is assumed carried to the abyssal floor in turbidity currents that only allow resedimentation to begin when the slope of the sea floor decreases offshore to less than 1 % grade (Meiburg and Kneller, 2010). The sedimentation scheme produces a continental shelf,

a well-defined shelf break, and a continental slope. The various parameters of the sedimentation were tuned in order to reproduce the envelope of sediment: the shapes of the sea floor and the depth to bedrock.

2.2 Isostasy

Bedrock in the model floats isostatically, balancing the load from the crust and sediment against that of a hypothetical displaced mantle fluid. The buoyancy of the crust is affected by cooling of the upper mantle in a thermal boundary layer that thickens with the square root of time, allowing subsidence with increasing crustal age. The elevation of the crust relaxes toward the equilibrium value on an isostatic rebound timescale of 10^4 years. The passive margin model has no representation of crustal rigidity except for a numerical smoothing operation, which has a spatial range of 10–20 km.

2.3 Organic carbon and methane

The particulate organic carbon (POC) content of the continentally-derived sedimenting material is specified in the model when it hits the sea floor, as a function of water depth. In the passive margin simulation, sea level changes were imposed on the simulation, along with a correlated time-varying oxygen "state" of the ocean which drives changes in POC concentration and the chemistry of the organic matter, in particular its H/C ratio. The active margin simulation reaches steady state in only 10 Myr, which is shorter than the 140 Myr duration of the passive margin simulations, so geological sea level and ocean oxygenation changes are not imposed on the simulations here. Instead, the relative sea level for these simulations was varied by ±20 m on a cycle time of 1 Myr, representing local tectonic uplift and subsidence driven by the forces confronting the crust in this "turbulent" part of crustal geophysics. The impact of this stipulation can be assessed in a simulation called No_Sealevel with time-invariant sea level.

Biologically- and thermally-driven chemical reactions produce dissolved methane, CH_4, which interacts with the gas and hydrate phases depending on temperature and

pressure conditions. Respiration of POC first consumes pore water SO_4^{2-} until it is depleted, which occurs relatively shallow in the sediment column. Bacterial respiration of POC then produces CH_4 and CO_2. The maximum efficiency of CH_4 production from the organic carbon is set by redox balance according to the H/C ratio of the POC. Porewater DIC δ^{13}C data from (Sivan et al., 2007) constrain the methanogenesis to be about 50 % of respiration, which is a bit lower than the maximum set by the redox constraint, as if some of the molecular hydrogen intermediary reacts with oxidized mineral phases rather than dissolved CO_2 to produce methane.

As temperatures warm further, exceeding about 60 °C, petroleum is produced, if the H/C ratio in the POC exceeds a value of 1 (Hunt, 1995). Petrogenesis draws the H/C ratio down toward a value of 1. A fraction of this petroleum (10 %) is assumed to migrate upward with a velocity of 1 m per thousand years. If it reaches the biological zone (temperature less than about 50 °C) it can be respired, producing CH_4 and CO_2, similarly to respiration of POC.

Thermal methanogenesis begins at about 150 °C, producing CH_4, DIC, and DOC. Ultimately the CH_4 production is limited by hydrogen in POC, with POH/POC approaching 0 in the hottest sediments. Thermogenic DOC production is assumed to be limited by organic oxygen availability, and is produced in a stoiciometry of CH_2O (e.g. acetate). DOC is also released by "sloppy feeding" in the respiration zone, and it is consumed in the respiration zone (producing DIC and methane if SO_4^{2-} is not available) with the same rate constant as applied to migrated petroleum.

The CH_4 concentration is compared with the solubility of bubbles and hydrate, and allowed to form those phases if it exceeds supersaturation. Hydrate is stationary within the sediment but bubbles migrate, following an ad-hoc parameterization that redistributes CH_4 in bubbles into overlying grid cells. This parameterization was needed to prevent buildup of excessive bubble volumes throughout the deep sediment column, and although the details of how the transport occurs are sketchy and at any rate unresolved in the model, it seems clear that, in the absence of evaporates or permafrost,

most methane gas produced in the sediment column does manage to escape the sediment column eventually (Hunt, 1995).

Each time step, some fraction of the excess bubbles in a parcel of sediment is removed, and the methane it contained is instantaneously redistributed into the grid cells above it that are undersaturated in dissolved methane, following an exponential decay of the upward bubble flux as a function of height in the undersaturated zone. The decrease in upward flux with height determines a source flux of methane to the grid boxes above. Upward fluxes from multiple grid boxes in the sediment combine together, and the upward flux at the sea floor is considered loss from the sediment column. The methane inventory was found to be extremely sensitive to the scale height in the parameterization, and we will show similar sensitivity studies for the active-margin model with similar results.

3 Active model configuration

3.1 Reference case and variants

To understand and document how the model works we show results from a suite of model sensitivity runs summarized in Table 1. Details of these scenarios will be explained as the new components of the model relevant to the active margin setting are described. In contrast to the passive margin simulations, the grid resolution is the same for all of the active margin simulations presented here.

3.2 Deformation of the sediment column

In the active model configuration, in addition to the processes in the passive margin model, the model grid in the horizontal dimension is manipulated to simulate the uniform compaction and thickening of the sediment column by lateral compression. The x coordinate values of the grid cells are carried laterally by the moving crust, and the

spacing between the grid points decreases, resulting in uniform vertical thickening of the sediment column.

The velocity of the incoming sediment column in the offshore edge of the model domain (the right) is the crustal velocity, specified as a parameter of the model scenario (for which there are sensitivity runs Fast Plate and Slow Plate). The plate velocity is taken to be $40\,\mathrm{cm\,yr^{-1}}$, from the subduction rate of the Juan de Fuca plate. The Juan de Fuca ridge is not orthogonal to the direction of plate motion, nor is it geographically stationary, but rather is moving slowly toward the trench. The model formulation as presented here simplifies this geometry into two dimensions by equating the spreading and subduction velocities, maintaining a constant distance between the ridge and the subduction zone throughout the model simulation. This simplification affects the plate velocity and also the amount of sediment that enters the wedge through time, and its impact can be assessed from the sensitivity to plate velocity and to sedimentation (simulation Pelagic).

At the onshore end of the domain, the sediment column velocity is held fixed at a value 10 times lower than the incoming sediment column velocity, representing a sediment column nearly stopped by collision into the other plate. The rate is specified at an extrapolated x location at which the sea floor would rise above sea level. The velocities of the grid points offshore of this are determined by

$$u_{\mathrm{sedcol}_{n+1}} + u_{\mathrm{sedcol}_n} - K_{\mathrm{deform}} \frac{\Delta x}{\Delta z_{\mathrm{sedcol}}} (u_{\mathrm{plate}} - u_{\mathrm{sedcol}_n})$$

where K_{deform} is a dimensionless deformation constant that controls the horizontal extent of the wedge relative to the thickness of the incoming sediments. The velocities are negative because they flow in the direction of decreasing x (Fig. 1a). The horizontal extent of the deformation zone, in this simulation about $150\,\mathrm{km}$, is determined by the value chosen for K_{deform} (for which there is a sensitivity run called Wide Def).

The x coordinate (location in physical space) of each horizontal grid point is updated each time step according to its calculated velocity. As the sediment column slides landward, the state of the underlying ocean crust at the grid point is recalculated based

on its new location, including in particular the flexure effect of the subducting plate in the trench. The sediment column rides but also isostatically steers the pathway of the subsiding ocean crust, as it thickens vertically due to the convergence horizontally.

As grid points move across the $x = 0$ origin, or as the sediment column begins to outcrop from the ocean, they are dropped from the model domain, and a new grid point is created on the far right-hand side of the domain. These sediment columns are initialized with a computationally-required minimum $1\,\mathrm{m}$ thickness per each of 15 grid cells, a negligible fraction of the ultimate sediment wedge. The $400\,\mathrm{km}$ mark from the extrapolated coastline is taken to be the spreading center where ocean crust is created and begins to accumulate sediment. The grid points propagate through the domain, emerging on the right as new crust is formed at the spreading center, and accumulating sediment and deforming as they converge toward the left. The eventual model steady state has no stationary points in it, but it manages to reach a standing stationary solution.

By conservation of volume the thickness of the column $\Delta z_{\mathrm{sedcol}}$ increases as Δx decreases. The model is formulated in vertical columns, which mandates that the sediment column deforms strictly vertically. This has the effect of increasing the excess pressure in the fluid phase, driving an expulsion fluid flow (Yuan et al., 1994). Real sediment column compression is generally focused on diagonal faults in the column, with a block of sediment from one side of the fault over-riding the other by sliding upward along the fault. The faults can dip onshore (normal) or offshore (abnormal), perhaps depending on the frictional state of the contact with bedrock (Davis et al., 1983).

Fortunately, previous models of sediment accretion have found a strictly vertical formulation to be an acceptable approximation, for modeling heat flow (Wang et al., 1993) and mineral closure ages (Batt et al., 2001). The effect of slip motion along diagonal faults dipping in either direction would be to displace material laterally. A parcel of over-riding sediment over a fault dipping offshore, for example, would be moving shoreward somewhat as it rides the wedge upward toward shallow waters through the domain of the model. A parcel at the top of the undeformed incoming sediment column might

progress into the wedge a bit before a contemporaneous parcel from the bottom of the incoming column. But the lateral displacements ought to be limited by typical fault geometry to be not much larger than the thickness of the sediment column, 5–10 km or so. This is a small displacement relative to the overall width of the wedge, which is about 100 km. So we expect the effects of this mode of motion to be relatively small.

Ultimately the inventory of sediment in the model domain overall is determined by the balance of the sources and sinks, from lateral sediment advection into and out of the domain, and by sediment deposition from the adjacent continent. In the absence of deposition of new continental material, the factor of 10 difference in the velocities incoming and outgoing would ultimately drive the sediment column to contain 10 times more sediment per meter on the outgoing end, in the steady state (Fig. 2). Adding continental material drives the outgoing column higher yet. Choosing the factor by which to impede the outgoing sediment column velocity (the factor of 10) essentially sets the model domain; a value of 10 achieves a solution in which the sediment column is close to outcropping at the sea surface, encompassing the entire hydrate stability zone but missing the complexities of sediment transport and erosion that produce the continental shelf, and erosion on land.

The model as described so far produces a smooth continental slope, but the sea floor in accretionary zones in reality are ridged, as blocks ride over each other. We attempt to simulate the effect of topography in the wedge by varying the deformation constant laterally, by ± 40 % on a wavelength of 100 km, in a simulation called Bumpy. The zones of high and low deformability travel with the material through the domain, and new grid points are initialized by extrapolation, continuing the original wave into the new incoming model domain (Fig. 2).

3.3 Crustal bending

Near the subduction zone, an oceanic plate is pressed downward by the load of the subducted lithosphere on the other side. The lithosphere deforms elastically, with the flexural rigidity determining the bending in response to a given torque. The situation is

2975

analogous to a floating dock with a person ready to dive in, standing at the edge. There is a zone next to the diver where the lateral cohesion of the crust pulls it downward, and then inshore of this, the dock rises out of the water somewhat, due to the requirement for overall isostatic equilibrium, and to the stiffness of the dock.

This situation is treated in the model based on an analytical solution to the case of a single point load at the subduction zone (Turcott and Schubert, 1982). The differential equation is

$$D\frac{d^4 z}{dx^4} + (\phi_m - \phi_{sw})gz = 0$$

and its solution with application of appropriate boundary conditions

$$dz_{tq} = \sqrt{2} \cdot e^{\pi/4} \cdot z_b \cdot e^{-\frac{\phi \cdot x_s}{4}} \cdot \sin\left(\frac{\phi \cdot x_s}{4}\right)$$

where

$$x_s = \frac{x - x_0}{x_b - x_0}$$

There are three tunable parameters in this formulation (Fig. 1b). One, z_b, corresponds to the height above isostasy of the forearc bulge, for which we use 100 m. Two are horizontal space scales. One, x_0, is from the edge of the plate (where the guy is standing, $x = 0$) to the boundary between the trench and the bulge (defined as the local isostatic equilibrium $z = 0$ line). The other, x_b, is the coordinate at the peak of the bulge. We use 125 and 175 km, respectively. These horizontal scales have a huge impact on the eventual depth of the trench. The isostatic load of the sediment column, described next, greatly amplifies the eventual depth of bedrock in the trench. A "torque pulldown" of about 2000 meters at the left-hand side of the domain ultimately results in 10 km of trench (Fig. 2).

2976

3.4 Isostasy

The displacement of the crust near the subduction zone is implemented in the model as a deviation from the isostatic equilibrium condition to which the elevation of the crust relaxes. In this way, the mass of the sediment column still has an impact on the elevation of the crust, so that sedimentation can drive subsidence. The correct way to do this calculation would be to solve the differential Eq. (1) using the distributed load of the sediment column, allowing the load full interplay with the rigidity of the crust. SpongeBOB is formulated as a simpler approximation to this. The mass load effects the isostatic equilibrium value locally, without regard for the springiness of the crust, in order to benefit from the convenient analytical solution to the $x = 0$ point load case.

3.5 Sea level and time-dependent forcing

Because of the shorter simulation time (10 Myr) the 150 Myr sea level cycle, a fundamental driver to the passive margin simulations (Archer et al., 2012), was neglected. We do however incorporate a ±20 m sea level oscillation on a time scale of 1 Myr to simulate the turbulence that a tectonic regime must be experiencing. The sensitivity to this forcing is gauged by a simulation called No Sealevel.

3.6 Sediment erosion and landslides

The solution of the horizontal compression and deformation scheme, by itself, would tend toward ever-increasing sea floor slope in the shoreward direction (Fig. 3). This tendency is balanced in the model by slope erosion and landslides. The grade of the sea floor is limited to a critical value (6 % in the Base simulation) by two mechanisms. One is during sediment deposition; if the sea floor slope is supercritical the material that would have sedimented is instead added to a resuspended pool and advected offshore.

The other mechanism is an erosional term that is triggered when the sea floor slope exceeds critical. Sediment is removed from the top computational box by relaxation toward a value that would bring the grid point back to the critical slope with respect to its adjacent grid point, with a relaxation time constant of $10^{-5}\,\mathrm{yr}^{-1}$, sufficiently fast to hold the sea floor close to the critical value, but slow enough to be kind to the numerics of the model. Solid material and pore fluid are advected upward through the computational grid, allowing the grid during erosion events to contract as the sediment column erodes.

The resuspended material is assumed incorporated into a turbidity current that travels down slope without deposition of sediment until the sea floor slope is less than 1 %. Beginning at this point, the resuspended sediment deposits on the sea floor following the same criteria for deposition as used by the primary depositing continental material, with larger size classes falling out faster than small particles. The eroding material conserves the chemical and grain-size characteristics, but the redeposition of POC is fractionated by the size separation of the redepositing material. Snapshots of sediment accumulation/erosion rates and the fraction of redepositing material are shown in Fig. 4.

The POC is distributed, in the model as well as in observations (Mayer, 1994), according to the surface area of the sediment, such that smaller size classes have a higher POC content by weight, due to their larger surface to volume (mass) ratio. The size fractionation of the POC can move the zone of highest POC content offshore; in particular this is evident in the Broad simulation, which has a shallow critical slope angle and hence a lot of sediment redeposition (Fig. 5).

3.7 Pore fluid flow

Pore fluid flow in the model is driven by the accumulating mass of the sediment column, and governed by Darcy's law and a sediment permeability which depends on the grain size and the porosity of the local sediment. The derivation of excess pressure from the

porosity, and the numerical advection scheme including flow limiter, are described in the companion paper (Archer et al., 2012).

Most of the fluid flow from the real ocean sediment column appears to make its way through high-permeability channels and pathways rather than flowing homogeneously through the bulk sediment column. The SpongeBOB model is too coarsely gridded to resolve faults and sandy turbidites in detail, but the overall impact of flow heterogeneity on the geochemistry of the sediment column is mimicked by imposing a factor of 100 anisotrophic enhancement of horizontal (along-grid) flow, and creating vertical channels of high permeability within the SpongeBOB grid. The channels are placed every 5 model grid points, and their permeability is enhanced by a factor of 10 relative to the background grid points. The grid points are found to focus the upward flow, and result in significant changes in the pore water chemistry both within the channels and also in the background cells. For these active margin simulations, the permeable channels are carried horizontally with the computational grid, following the sediment material. Vertical flow velocities, relative to the sediment grains (Darcy flow, w_{Darcy}) and relative to the sea floor ($w_{seafloor}$) are shown in Fig. 6.

3.8 Heat flow

The heat flow results are shown in Fig. 7. The model captures the general trend of lower heat fluxes onshore, and by about the same magnitude of drawdown. The model fluxes are lower than the measurements from Hyndman and Wang (1993), driven by a model geothermal heat flow of $100\,mW\,m^{-2}$, compared to the offshore heat flux of 120–$130\,mW\,m^{-2}$ in the data. The diffusive heat flow values are impacted by the permeable vertical channels, which appear as spikes of high heat flux. The simulations all appear to parallel each other in their decreasing heat flow with sediment column thickening, and parallel the trend in the data. The one curious model result comes from the Broad scenario, in which a shallow critical slope angle drives high rates of sediment erosion and redeposition (Fig. 7b, dashed lines). In this scenario, removal of sediment by ero-

sion increases the heat flux landward, counteracting the decrease landward seen in all the other simulations (and the data).

3.9 Organic carbon and methane

The model respiration and thermal degradation kinetics are the same as in the companion paper (Archer et al., 2012). The production rates of methane from respiration and thermal degradation are shown in Fig. 8. Methane concentrations from the simulations are shown in Fig. 9. Bubbles are shown in Fig. 10, and hydrate in Fig. 11. The simulations are similar to the eye, but variations can be seen in the envelope of the sediment column, for example, due to plate velocity (Fast Plate and Slow Plate), sediment column deformation (Wide Def and Bumpy), and sediment transport and reposition (Pelagic and Broad Slope). Methanogenesis rates are affected by the labile fraction of POC (Bio 10 % and Bio 100 %), impacting the distribution of dissolved methane, bubbles, and hydrate.

Stable carbon isotopes provide a diagnostic window into the dynamics of the sedimentary carbon cycle. Profiles of the $\delta^{13}C$ of dissolved methane and dissolved inorganic carbon (DIC) from the Base case are compared with the measurements of Pohlman et al. (2009) in Fig. 12, and results from the other scenarios are plotted in Figs. 13 and 14. The primary driver of the isotopic compostions in the model is the efficiency with which POC is converted to methane as opposed to DIC. Variations in the model geophysical scenarios do not have a major impact on the isotopic compositions.

In broad brush the model captures the general isotopic compositions as measured, but the field data show a systematic dependence of the isotopic compositions that is not found in the model results. The isotopic compositions of both species are systematically heavier in the middle of the deformation wedge than they are near the toe of the wedge (water depths ranging from 2200 meters near the two to about 1000 m at their innermost profile). The heavier isotopic compositions could be explained as a gradient in the efficiencies of POC conversion into CH_4 relative to DIC. For example, if the source POC is −25‰, and the fraction on CO_2 reduction −60‰, then a conversion ef-

ficiency of POC to CH$_4$ of 25 % would explain the isotopic compositions of both tracers at the toe of the deformation zone, and an increase to 75 % methanogenesis efficiency would explain the measurements in the mid-wedge. The low efficiency at the toe would have to be explained as the impact of sulfate reacting with CH$_4$, while the high values in the mid wedge would require highly reduced organic carbon as a source, with an H/C ratio of at least 2, or perhaps an inorganic source of dissolved hydrogen to react with DIC.

4   Model sensitivities

Figure 15 shows the hydrate inventories of all the simulations, and the results are digested into specific model sensitivities in Fig. 16. The temperature of the ocean does affect the inventory of methane hydrate (Fig. 16a), although the temperature sensitivity of this and the passive margin model are both lower than that of the one-dimensional Davie and Buffett (2001) model as deployed globally by Buffett and Archer (2004). The degradation kinetics of POC (Fig. 16b) have a much stronger impact on the inventory of methane hydrate, as we also found for the passive margin simulations. And, also in common with the passive margin simulations, the ability of the sediment column to recapture rising bubbles, manifested in a bubble redissolution scale height, has a very strong impact (Fig. 16c).

The most interesting new result from these simulations is the role of subduction in the methane cycle, and its sensitivity to the subduction velocity of the incoming plate (Fig. 16d). In general, the hydrate concentrations (filled fraction of pore volume) are higher in the active margin simulation than they are in the passive margin simulation, with a full-scale of 10 % for these plots but only 5 % for the hydrate concentrations in the passive margin companion paper. However, but the inventories of hydrate per meter of coastline are lower than the passive margin simulation (indicated in Fig. 16d as 0 plate velocity), and faster plate motion decreases the inventory of hydrate at the end of the simulation, everything else being equal. Perhaps this effect is due to the uplifting of the

surface sediment due to the sediment convergence in the accreting wedge, continually depleting the stability zone of methane hydrate by advecting sediment through the stability zone. The highest hydrate saturations tend to be found at the toe of the wedge, similarly to observations from Cascadia (Malinverno et al., 2008).

Other insights into the functioning of the model can be gleaned by examination of a few more of the simulation results in Fig. 15. The vertical permeable channels have only a minor impact on the overall abundance of methane hydrate (No Chan), in contrast with the passive margin simulation, in which the elimination of the channels decreased the hydrate inventory by about a factor of two. Thermogenic methane production is also found to be unimportant to methane hydrates (No Therm). Thermal methanogenesis alters the δ^{13}C of methane in the deep sediment column, but it has limited impact on compositions in the shallower sediment column (Fig. 13). Most of the geophysical variants had only a small impact on the hydrate abundance, for example the heterogeneous deformation scenario Bumpy, the altered sedimentation scheme Pelagic, or the No Erod scenario which prohibits sediment erosion. The one exception to this lack of sensitivity to model geophysical formulation is that the two scenarios with generally larger sediment envelopes, Slow Plate and Broad Slope (which erodes more aggressively to maintain a shallower sea floor slope than the base case) both have more hydrate per meter of coastline than the other cases. The simulation No Sealevel shows that the fluctuations in sea level that are imposed on the Base case had little effect on the hydrate inventory.

5   Conclusions

Active margin coastal settings tend to have high concentrations of methane hydrate in surface and near-surface sediments, leading to a conceptualization of intense methane delivery to surface sediments by pore fluid flow, driven by the deformation of the thick sediment wedge. Our model confirms the general importance of geophysical forcing on the methane cycle in the wedge, but finds that horizontal motion of the sediment

through the wedge flushes hydrate out of the stability zone, decreasing the global inventory of methane hydrate (moles per meter of coastline) relative to the case of no subduction (the passive margin).

Other uncertainties to which the hydrate inventory of the model are most sensitive echo the findings of the passive margin simulations in the companion paper (Archer et al., 2012). The model is sensitive to ocean temperature but less so than 1-D models of the near-surface sediment, probably due to the incorporation of bubble transport of methane included in this model but neglected in the smaller domain models. The bubble transport parameterization of the model has an enormous impact on hydrate inventories, providing incentive for future work to characterize the appropriate value for this parameter for bubbles in the real sediment column. The sensitivity of the models to POC degradation rate also appears to be stronger than that for temperature. Discussion of the possibility of hydrate degassing events in Earth's history, for example the PETM, has generally been based on the idea that there would be less hydrate in a warmer world (Archer, 2007). However, it could be that higher organic carbon deposition rates in a hothouse climate could more than offset the impact of warmer temperatures on the hydrate inventory at that time.

In general, the model inventories of methane hydrate are still sensitive enough to uncertain parameters that the models provide no real strong new constraint on methane inventories of the real ocean, but rather the models can hope to diagnose what the sensitivities of the real ocean hydrate reservoir might be.

Supplementary material related to this article is available online at: http://www.biogeosciences-discuss.net/9/2967/2012/ bgd-9-2967-2012-supplement.zip.

References

Archer, D.: Methane hydrate stability and anthropogenic climate change, Biogeosciences, 4, 521–544, doi:10.5194/bg-4-521-2007, 2007.

Archer, D. E., Buffett, B. A., and McGuire, P. C.: A two-dimensional model of the passive coastal margin deep sedimentary carbon and methane cycles, Biogeosciences Discuss., 9, 2921–2966, doi:10.5194/bg-9-2921-2012, 2012.

Batt, G. E.: Tectonic synthesis of the Olympic Mountains segment of the Cascadia wedge, using two-dimensional thermal and kinematic modeling of thermochronological ages, J. Geophys. Res.-Solid Earth, 106, 26731–26746, 2001.

Buffett, B. and Archer, D. E.: Global inventory of methane clathrate: Sensitivity to changes in environmental conditions, Earth Planet. Sci. Lett., 227, 185–199, 2004.

Carson, B., Suess, E., and Strasser, J. C.: Fluid-Flow and Mass Flux Determinations at Vent Sites on the Cascadia Margin Accretionary Prism, J. Geophys. Res.-Solid Earth Planet., 95, 8891–8897, 1990.

Davie, M. K. and Buffett, B. A.: A numerical model for the formation of gas hydrate below the seafloor, J. Geophys. Res., 106, 497–514, 2001.

Davis, D., Suppe, J., and Dahlen, F. A.: Mechanics of fold-and-thrust belts and accretionary wedges, J. Geophys. Res., 88, 1153–1172, 1983.

Hunt, J. M.: Petroleum Geochemistry and Geology, 743 pp., Freeman, New York, USA, 1995.

Hyndman, R. D. and Wang, K.: Thermal Constraints on the Zone of Major Thrust Earthquake Failure – the Cascadia Subduction Zone, J. Geophys. Res.-Solid Earth, 98, 2039–2060, 1993.

Malinverno, A., Kastner, M., Torres, M. E., and Wortmann, U. G.: Gas hydrate occurrence from pore water chlorinity and downhole logs in a transect across the northern Cascadia margin (Integrated Ocean Drilling Program Expedition 311), J. Geophys. Res.-Solid Earth, 113, B08103, doi:10.1029/2008JB005702, 2008.

Mayer, L. M.: Surface area control of organic carbon accumulation in continental shelf sediments, Geochim. Cosmochim. Acta, 58, 1271–1284, 1994.

Meiburg, E. and B. Kneller, Turbidity currents and their deposits, Ann. Rev. Fluid Mech., 42, 135–156, 2010.

Milkov, A. V.: Global estimates of hydrate-bound gas in marine sediments: how much is really out there?, Earth-Sci. Rev., 66, 183–197, 2004.

Pohlman, J. W., Kaneko, M., Heuer, V. B., Coffin, R. B., and Whiticar, M.: Methane sources and production in the northern Cascadia margin gas hydrate system, Earth Planet. Sci. Lett., 287, 504–512, 2009.

Sivan, O., Shrag, D. P., and Murray, R. W.: Rates of methanogenesis and methanotrophy in deep-sea sediments, Geobiology, 5, 141–151, 2007.

Spence, G. D., Hyndman, R. D., Chapman, N. R., Walia, R., Gettrust, J., and Edwards, R. N.: North Cascadia deep sea gas hydrates, in Gas Hydrates: Challenges for the Future, 65–75, 2000.

Turcott, D. L. and Schubert, G.: Geodynamics, 472 pp., Cambridge University Press, Cambridge, UK, 1982.

Wang, K., Hyndman, R. D., and Davis, E. E.: Thermal Effects of Sediment Thickening and Fluid Expulsion in Accretionary Prisms – Model and Parameter Analysis, J. Geophys. Res.-Solid Earth, 98, 9975–9984, 1993.

Yuan, T., Spence, G. D., and Hyndman, R. D.: Seismic Velocities and Inferred Porosities in the Accretionary Wedge Sediments at the Cascadia Margin, J. Geophys. Res.-Solid Earth, 99, 4413–4427, 1994.

Table 1. Summary of model simulations.

Model Name	Description
Base	Baseline scenario
Bio 10 % Bio 100 %	Variation in the defined labile fraction of POC, 10 % and 100 % respectively, within the context of the Base case which takes 50 %
$T-2$ $T+2$ $T+4$	Effect of ocean temperature, changes of $-2\,°C$, $2\,°C$, and $4\,°C$
No Bubb Mig	Bubble migration disabled
Bubb 100 m Bubb 2 km	Bubble redissolution scale height of 100 meters and 2 km, relative to the Base case of 500 m
Fast Plate Slow Plate	Plate subduction velocity of 80 or $20\,mm\,yr^{-1}$ instead of the Base case of $40\,mm\,yr-1$. Slow plate simulation spun up for 20 Myr instead of Base 10 Myr.
Broad Slope	Critical seafloor slope of 2 % instead of default 6 %
Bumpy	Heterogeneous sediment deformation constant imposed as 100 km variations of 40 % in the deformation constant.
Wide Def	Decreased sediment deformation constant, spreading the deformation zone from 8×10^{-2} in the Base scenario to a value of 4×10^{-2}. The change diminishes the need for erosion to maintain a critical seafloor slope
Pelagic	Sedimentation dominantly "pelagic" (spatially uniform) rather than continentally derived (doubled pelagic, halved continental)
No Erode	Erosion disabled
No Thermogen	Thermogenic methane production disabled
No Chan	No vertical low-permeability chimneys.
No Sealevel	Sea level oscillations of $\pm20\,m$ on 1 myr time cycle in Base simulation disabled here

a

b
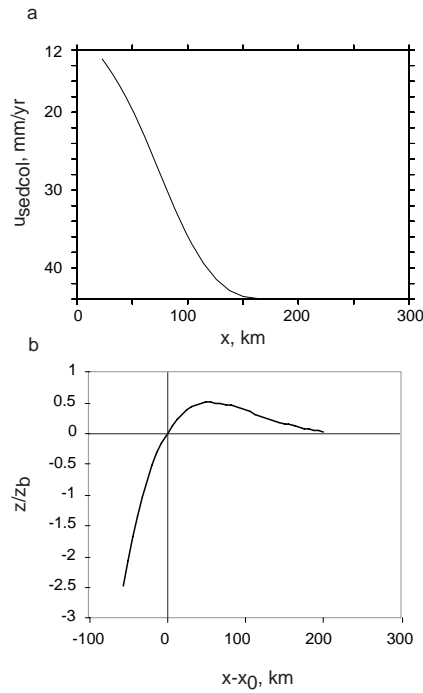
Fig. 1. (A) The sediment column velocity (negative meaning from right to left) for the *Base* scenario. **(B)** The solution to the plate flexure / isostasy balance near the subducting margin.

a

b

c

d
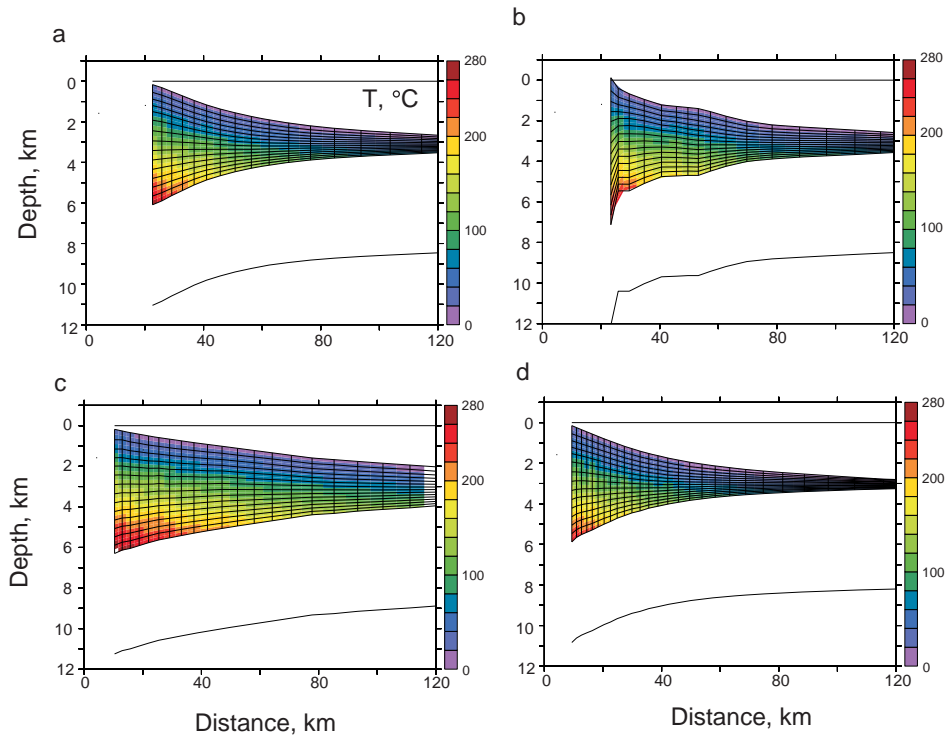
Fig. 2. Grid, temperature, and isostasy results for **(A)** *Base*, **(B)** *Bumpy*, **(C)** *Broad Slope*, and **(D)** *Fast Plate* scenarios. A movie of the Base scenario can be seen at http://geosci.uchicago. edu/~archer/spongebob_active/fig2.active.movie.gif and in the Supplement.
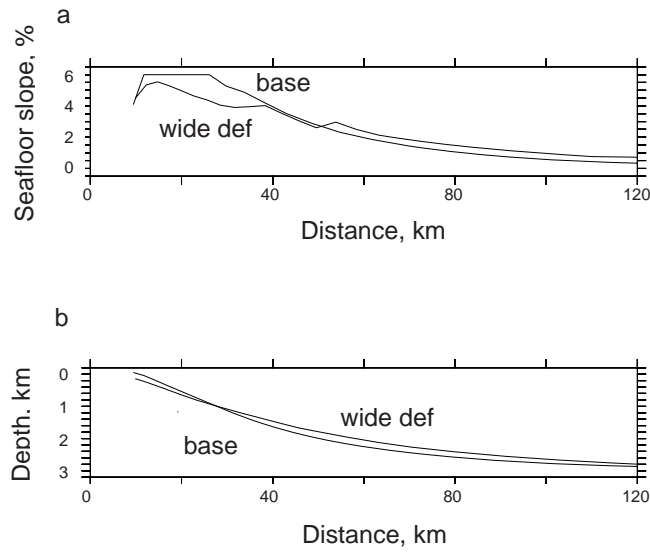
**Fig. 3. (A)** Sea floor slope and **(B)** sea floor depth for the *Base* and *Wide Def* simulations. *Wide Def* never reaches the critical sea floor slope of 6 %, and so the slope gets monotonically steeper as the simulation approaches the shore.
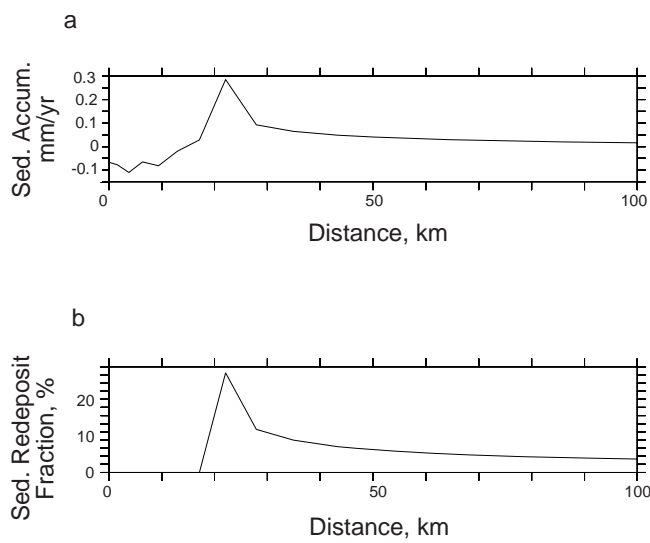
Fig. 4. (A) Total sediment accumulation rate and **(B)** redeposition fraction for the *Base* scenario.
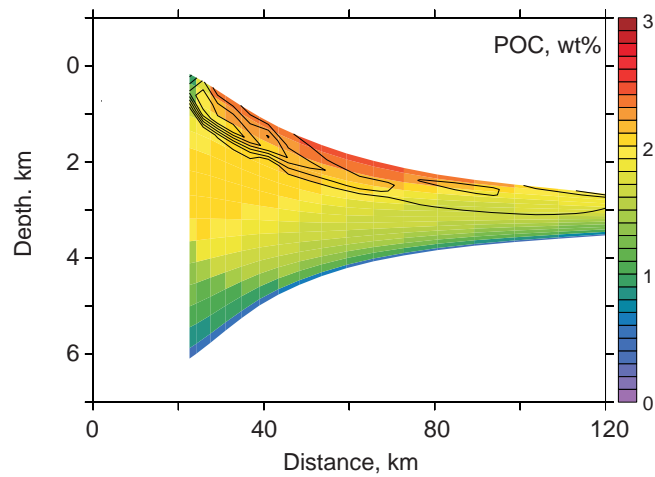
Fig. 5. POC results from the base case, with 12 cases as labeled plotted in Fig. 5 (Supplement). Contours are respiration rates. A movie of the *Base* and *Bumpy* simulations can be seen at http://geosci.uchicago.edu/~archer/spongebob_active/fig5.active.movie.gif and in the Supplement.
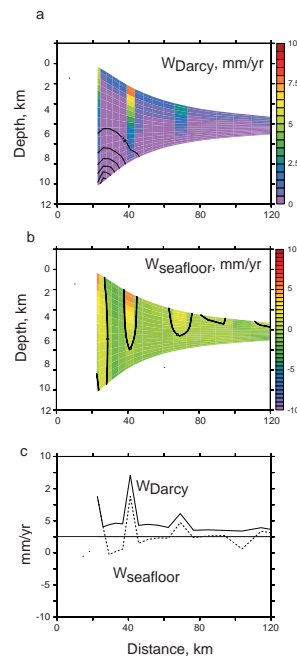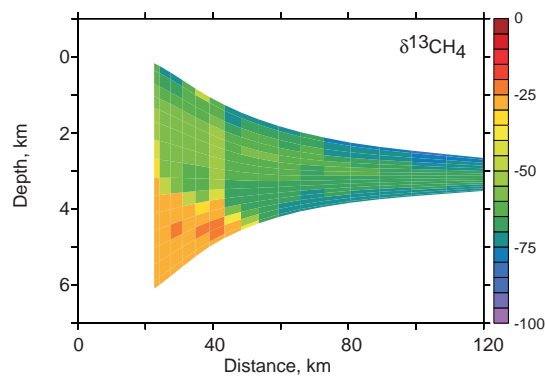
Fig. 6. (A) Sections of Darcy vertical velocities (flow relative to the grains), and **(B)** velocities relative to the sea floor, and **(C)** plots of w_{Darcy} and $w_{seafloor}$ at the sea floor, for the base scenario. Snapshots of other cases are shown in Fig. 6 Suppl (*Base*, *Bumpy*, *No Chan*, and *No Erod*). Movies of $w_{seafloor}$ from the Base and Bumpy scenarios can be seen at http://geosci.uchicago.edu/~archer/spongebob_active/fig6a.active.movie.gif and velocities at the sea floor at http://geosci.uchicago.edu/~archer/spongebob_active/fig6b.active.movie.gif and in the Supplement.
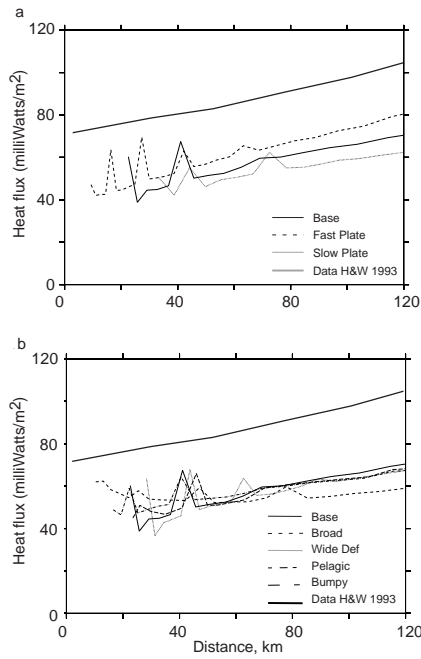
Fig. 7. Diffusive heat flow results compared with data from Hyndman and Wang (1993). **(A)** and **(B)** are various model scenarios as indicated.
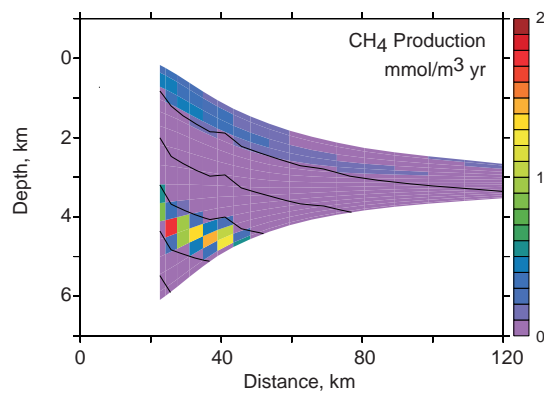
Fig. 8. Methanogenesis rates in the base scenario. Results from other scenarios shown in Fig. 8 (Supplement) Shallow is from biological activity, deep is thermogenic methane production rates. Contours are temperature. An animation can be seen at http://geosci.uchicago.edu/~archer/spongebob_active/fig8.active.movie.gif and in the Supplement.
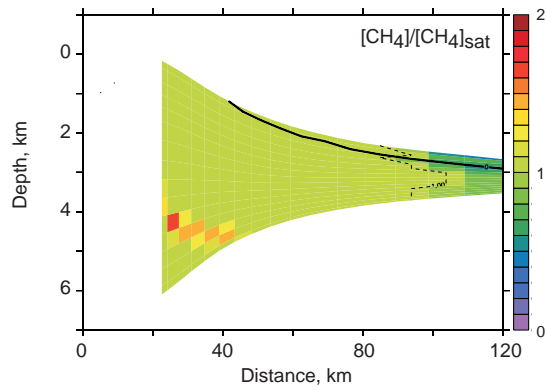
Fig. 9. Dissolved methane concentration relative to equilibrium with respect to gas (below the stability horizon, solid black line) or hydrate (above the stability horizon), for the base scenario, with additional scenarios in Fig. 9 (Supplement). An animation can be seen at http://geosci.uchicago.edu/~archer/spongebob_active/fig9.active.movie.gif and in the Supplement.
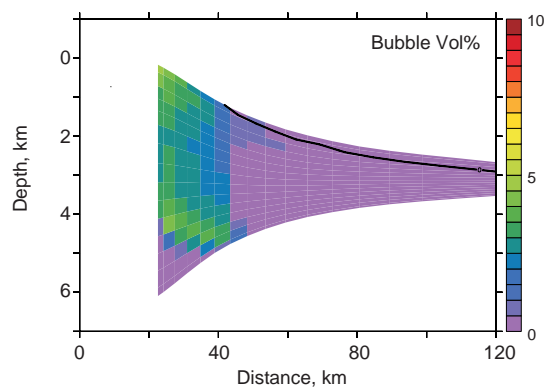
Fig. 10. Bubble concentration (percent pore volume) for the base scenario, with various other scenarios in Fig. 10 (Supplement). Solid black line is the hydrate stability boundary. An animation of the *Base* and *Bumpy* scenarios can be seen at http://geosci.uchicago.edu/~archer/spongebob_active/fig10.active.movie.gif and in the Supplement.

Fig. 11. Methane hydrate concentration, percent pore volume, for the base scenario. Solid black line is the stability boundary. Plotted with various other scenarios in Fig. 11 Supplemental. Animations of the Base and Bumpy scenarios can be seen at http://geosci.uchicago.edu/~archer/spongebob_active/fig11a.active.movie.gif and of the three plate speed scenarios at http://geosci.uchicago.edu/~archer/spongebob_active/fig11b.active.movie.gif and in the Supplement.

Fig. 12. Carbon isotopic compositions compared with measurements from Pohlman et al. (2009). Short dashes are near the toe, long dashes intermediate, and solid lines are closest inshore. Heavy lines are data, thin lines are model results.

Fig. 13. Carbon isotopic composition, $\delta^{13}C$, of dissolved methane, for the base scenario, with various other scenarios in Fig. 13 Supplemental. An animation of $\delta^{13}C$ of methane and DIC (Fig. 14) can be seen at http://geosci.uchicago.edu/~archer/spongebob_active/fig13-14.active. movie.gif and in the Supplement.
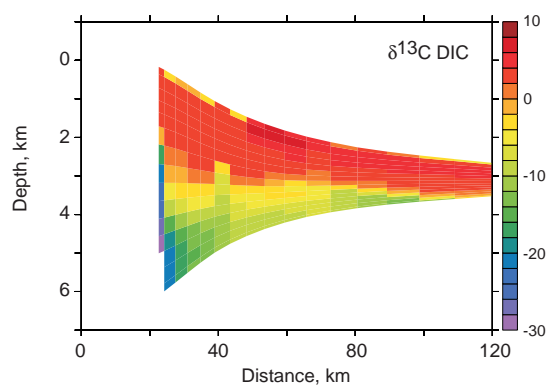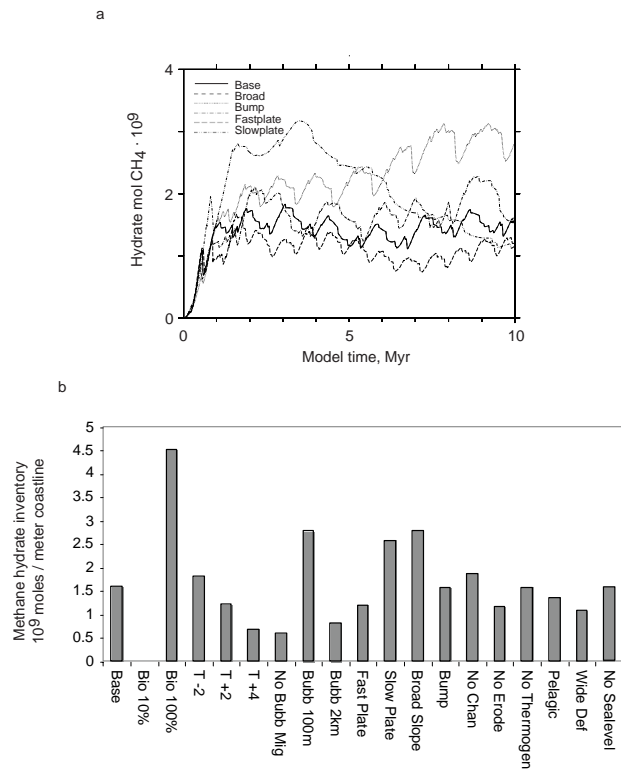
Fig. 14. Carbon isotopic composition, $\delta^{13}C$, of dissolved inorganic carbon, for the base scenario, with various other scenarios in Fig. 14 (Supplement). An animation of $\delta^{13}C$ of methane and DIC (Fig. 14) can be seen at http://geosci.uchicago.edu/~archer/spongebob_active/fig13-14.active.movie.gif and in the Supplement.

a

b

Fig. 15. (A) Time-dependent evolution of the scenarios showing variability due mostly to the coarse grid resolution. **(B)** Inventory of methane hydrate at the ends of the simulations for all model scenarios.
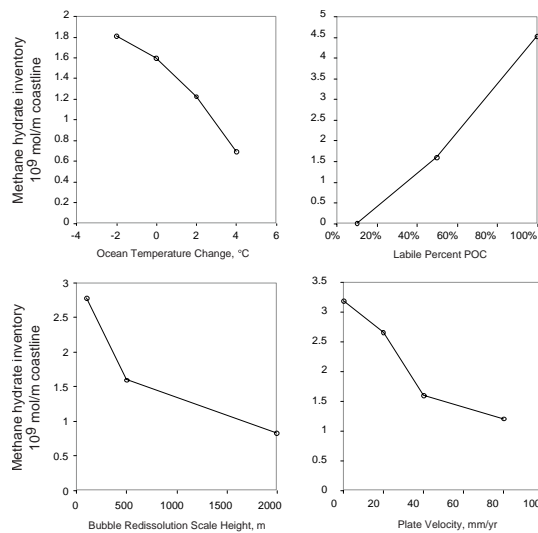
Fig. 16. Summary of model sensitivities: **(A)** Ocean temperature, **(B)** labile fraction of POC, **(C)** bubble redissolution scale height, **(D)** plate velocity (with zero velocity case taken from the passive margin simulation (Archer et al., 2012).